

This is a repository copy of *Development of Antiferromagnetic Heusler Alloys for the Replacement of Iridium as a Critically Raw Material*.

White Rose Research Online URL for this paper:
<https://eprints.whiterose.ac.uk/id/eprint/119935/>

Version: Published Version

Article:

Hirohata, Atsufumi orcid.org/0000-0001-9107-2330, Huminiuc, Teodor, Sinclair, John et al. (18 more authors) (2017) Development of Antiferromagnetic Heusler Alloys for the Replacement of Iridium as a Critically Raw Material. *Journal of Physics D: Applied Physics*. 443001. pp. 1-15. ISSN 1361-6463

Reuse

This article is distributed under the terms of the Creative Commons Attribution (CC BY) licence. This licence allows you to distribute, remix, tweak, and build upon the work, even commercially, as long as you credit the authors for the original work. More information and the full terms of the licence here:
<https://creativecommons.org/licenses/>

Takedown

If you consider content in White Rose Research Online to be in breach of UK law, please notify us by emailing eprints@whiterose.ac.uk including the URL of the record and the reason for the withdrawal request.

TOPICAL REVIEW • OPEN ACCESS

Development of antiferromagnetic Heusler alloys for the replacement of iridium as a critically raw material

To cite this article: Atsufumi Hirohata *et al* 2017 *J. Phys. D: Appl. Phys.* **50** 443001

View the [article online](#) for updates and enhancements.

Related content

- [Exchange bias effects in Heusler alloy Ni₂MnAl/Fe bilayers](#)
Tomoki Tsuchiya, Takahide Kubota, Tomoko Sugiyama *et al.*
- [Mn₂VAl Heusler alloy thin films: appearance of antiferromagnetism and exchange bias in a layered structure with Fe](#)
Tomoki Tsuchiya, Ryota Kobayashi, Takahide Kubota *et al.*
- [Future perspectives for spintronic devices](#)
Atsufumi Hirohata and Koki Takanashi

Recent citations

- [Crystal and magnetic structure of antiferromagnetic Mn₂PtPd](#)
Vivek Kumar *et al*
- [Critical raw materials cluster](#)
M P Chamberlain



IOP | ebooks™

Bringing you innovative digital publishing with leading voices to create your essential collection of books in STEM research.

Start exploring the collection - download the first chapter of every title for free.

Topical Review

Development of antiferromagnetic Heusler alloys for the replacement of iridium as a critically raw material

Atsufumi Hirohata¹, Teodor Humeniuc², John Sinclair², Haokaifeng Wu², Marjan Samiepour¹, Gonzalo Vallejo-Fernandez², Kevin O'Grady², Jan Balluf³, Markus Meinert³, Günter Reiss³, Eszter Simon⁴, Sergii Khmelevskiy⁵, Laszlo Szunyogh^{4,6}, Rocio Yanes Díaz⁷, Ulrich Nowak⁷, Tomoki Tsuchiya⁸, Tomoko Sugiyama⁸, Takahide Kubota^{8,9}, Koki Takanashi^{8,9}, Nobuhito Inami¹⁰ and Kanta Ono¹⁰

¹ Department of Electronic Engineering, University of York, Heslington, York YO10 5DD, United Kingdom

² Department of Physics, University of York, Heslington, York YO10 5DD, United Kingdom

³ Department of Physics, University of Bielefeld, Universitätsstraße 25, 33615 Bielefeld, Germany

⁴ Department of Theoretical Physics, Budapest University of Technology and Economics, Budafoki út 8, 1111 Budapest, Hungary

⁵ Center for Computational Materials Science, Institute for Applied Physics, Vienna University of Technology, Wiedner Hauptstrasse 8, A-1060 Vienna, Austria

⁶ MTA-BME Condensed Matter Research Group, Budapest University of Technology and Economics, Budafoki út 8., H-1111 Budapest, Hungary

⁷ Department of Physics, University of Konstanz, Postfach 674, 78457 Konstanz, Germany

⁸ Institute for Materials Research, Tohoku University, 2-1-1 Katahira, Sendai 980-8577, Japan

⁹ Center for Spintronics Research Network, Tohoku University, 2-1-1 Katahira, Sendai 980-8577, Japan

¹⁰ Institute of Materials Structure Science, High Energy Accelerator Research Organization (KEK), 1-1 Oho, Tsukuba 305-0801, Japan

E-mail: atsufumi.hirohata@york.ac.uk

Received 9 June 2017, revised 28 July 2017

Accepted for publication 29 August 2017


Published 27 September 2017



CrossMark

Abstract

As a platinum group metal, iridium (Ir) is the scarcest element on the earth but it has been widely used as an antiferromagnetic layer in magnetic recording, crucibles and spark plugs due to its high melting point. In magnetic recording, antiferromagnetic layers have been used to pin its neighbouring ferromagnetic layer in a spin-valve read head in a hard disk drive for example. Recently, antiferromagnetic layers have also been found to induce a spin-polarised electrical current. In these devices, the most commonly used antiferromagnet is an Ir–Mn alloy because of its corrosion resistance and the reliable magnetic pinning of adjacent ferromagnetic layers. It is therefore crucial to explore new antiferromagnetic materials without critical raw materials. In this review, recent research on new antiferromagnetic Heusler alloys and their exchange interactions along the plane normal is discussed. These new antiferromagnets are characterised by very sensitive magnetic and electrical measurement techniques recently developed to

 Original content from this work may be used under the terms of the [Creative Commons Attribution 3.0 licence](https://creativecommons.org/licenses/by/3.0/). Any further distribution of this work must maintain attribution to the author(s) and the title of the work, journal citation and DOI.

determine their characteristic temperatures together with atomic structural analysis. Mn-based alloys and compounds are found to be most promising based on their robustness against atomic disordering and large pinning strength up to 1.4 kOe, which is comparable with that for Ir–Mn. The search for new antiferromagnetic films and their characterisation are useful for further miniaturisation and development of spintronic devices in a sustainable manner.

Keywords: critical raw materials, platinum group metals, iridium replacement, antiferromagnetic Heusler alloys

(Some figures may appear in colour only in the online journal)

1. Introduction

The European Commission identified 14 critical raw materials (CRMs) in 2011 and revised to 20 CRMs three years later [1]. These include antimony, beryllium, borates, chromium, cobalt, coking coal, fluor spar, gallium, germanium, indium, magnesite, magnesium, natural graphite, niobium, phosphate rock, platinum group metals (PGMs), heavy rare earth elements, light rare earth elements, silicon metal and tungsten. Similar lists have been made also by other governments such as those of the USA, Japan and China. As a measure of criticality, a sustainability index (SI) has been introduced to assess the difficulty in substituting the material, scored and weighted across all applications. SI values are between 0 and 1, with 1 being the least substitutable. Among these CRMs, phosphate rock has the highest SI of 0.98, followed by the SIs of chromium, borates, germanium, beryllium and PGMs of 0.96, 0.88, 0.86, 0.85 and 0.83, respectively. Generally, the PGMs have a relatively high end-of-life recycling input rate of 35%, which is a measure of the proportion of metal and metal products that are produced from end-of-life scrap and other metal-bearing low grade residues in end-of-life scrap worldwide. Even so, among the PGMs, only 1–2% in Pt and Rh ore contains iridium and 87% of the Ir world supply (~5.8 t in 2011 [2]) is from South Africa. This makes Ir to be the scarcest element on the earth with the composition of 4×10^{-4} ppm, which is almost one (or more) order of magnitude less than the other PGMs, e.g. Pt (3.7×10^{-3} ppm) and Ru (1×10^{-3} ppm).

In general, the PGMs have very high melting point (>1800 K) due to their crystalline stability. Especially, Ir has one of the highest melting points of 2739 K. Hence, due to its stability, Ir (and its alloys) has been used as a prototype kilogram, a prototype metre, and for spark plugs, dip pens, rings and tooth fillings. In addition to these traditional usages, electrical and electrochemical applications of Ir have been increasing over the last decades, resulting in the worldwide demand of 7.7 t in 2016 [3]. Such a high demand is responsible for the severe fluctuation in Ir price over the last decade as shown in figure 1 [4]. Until the beginning of 2007, the Ir price was almost stable to be approximately USD 5/g. However, it took the maximum of USD 35/g in 2011 with over 130% fluctuations. Since the middle of 2016, it has been monotonically increasing again to USD 30/g, approaching the maximum price. These fluctuations are caused by the above demand greater than the supply and the associated speculation.

Among the heavy demands, electrical and electrochemical applications are the two major sectors. For the electrical use (2.1 t worldwide in 2017), antiferromagnetic (AF) Ir–Mn alloys for magnetic memory and Ir-complex for organic electroluminescence (EL) are major applications. For organic EL, tridentate [5] and bidentate Ir-complex [6] are used to generate red, blue, yellow and green EL. To avoid the usage of Ir, carbazoyl dicyanobenzene has been demonstrated to exhibit EL with these colours with 100% efficiency [7]. For the electrochemical use (1.8 t worldwide in 2017), on the other hand, crucibles for sapphire glass production has been increasing the demands recently due to the sapphire glass usages for mobile phones and tablet computers. The used crucibles can be recycled by fragmentation of metal scraps [8]. The metal scraps are dissolved in aqua regia ($\text{HNO}_3 + 3\text{HCl}$), followed by the introduction to PbO solvent and HNO_3 , NaHSO_4 and Na_2O_2 in series. The residual solution is then purified as $(\text{NH}_4)_3[\text{IrCl}_6]$, which can be reduced by H_2 gas to Ir. Hence, it is important to develop a replacement for Ir alloys used in magnetic memory industry, which has no sustainable solution to date.

In this paper, we review the recent development of AF materials consisting of abundant elements to replace Ir as a CRM. Due to the corrosion resistance for device applications, we focused on AF Heusler alloys. We have established correlations between their crystalline structures and magnetic properties, i.e. antiferromagnetism. Heusler alloys consisting of elements with moderate magnetic moments require perfectly or partially ordered crystalline structures to exhibit AF behaviour. By using elements with large magnetic moments, even a fully disordered structure is found to show either AF or ferrimagnetic (FI) behaviour. The latter alloys may become useful for device applications by additional increase of their anisotropy and grain volume to maintain the AF behaviour above room temperature (RT).

2. Antiferromagnetic materials

AF materials have been investigated intensively both theoretically and experimentally since the initial discovery by Louis Néel [9]. For example, Mn–O exhibits AF behaviour due to the antiparallel alignment of Mn magnetic moments [10] via their superexchange interactions [11]. Due to the antiparallel alignment of the moments with the same amplitude, it is very difficult to characterise the AF behaviour using macroscopic measurements. Accordingly, a ferromagnet (FM)/AF bilayer

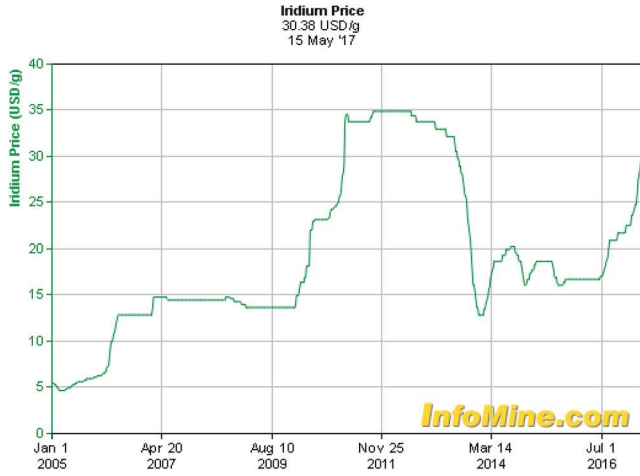


Figure 1. Recent iridium price in USD/g [4].

has been introduced to induce interfacial exchange coupling to pin the magnetisation of the FM layer. This results in a shift in the corresponding magnetisation curve, which is known as exchange bias field H_{ex} , along a magnetic field applied [12]. In such a bilayer, the AF properties, e.g. anisotropy and temperature dependence, can be indirectly characterised by measuring H_{ex} due to the interfacial FM/AF coupling. From the device application point of view, H_{ex} can pin one of the FM magnetisations in a FM/non-magnet (NM)/FM trilayer, providing a spin-valve structure [13]. The spin-valve is a basic building block for a read head of a hard disk drive (HDD), which is the most common data storage recording almost 85% of the information produced by human being. By replacing the NM layer with an insulating barrier, a magnetic tunnel junction (MTJ) can also be fabricated in a similar manner. Such MTJs are used as the latest HDD read head and a data bit cell of a magnetic random access memory (MRAM). Recently, by flowing an electrical current in an AF layer, spin polarisation has been demonstrated to be induced, leading to AF spintronics [14]. For these spintronic applications, an IrMn_3 alloy has been predominantly used due to its corrosion resistance and robustness against device fabrication processes in nanometre-scale in both thickness and in-plane dimensions (see table 1 for major AF materials).

In an AF material, the antiparallel alignment of the magnetic moments becomes random to transform into paramagnetism with increasing temperature above a magnetic transition temperature as known as the Néel temperature (T_N). This can be explained by applying the Weiss field onto independent A and B sites, which have antiparallel alignment as shown in figure 2 (for $x \ll 1$) [17]. The magnetisation of these sites (M_A and M_B) can be determined as

$$\begin{cases} M_A = \frac{1}{2}Ng\mu_B JB_J(x_A) = \frac{Nm^2}{6k_B T} H_A = \frac{C}{2T} H_A \\ M_B = \frac{1}{2}Ng\mu_B JB_J(x_B) = \frac{Nm^2}{6k_B T} H_B = \frac{C}{2T} H_B \end{cases}, \quad (1)$$

where N is the number of magnetic moments, g is Lande's g -factor, μ_B is the Bohr magneton in a unit volume, J is the angular momentum number, B_J is the Brillouin function for $x_{A(B)}$ [$= (g\mu_B J/k_B T) H_{A(B)}$], m is the magnetic moment, k_B is the Boltzmann constant, T is temperature, H is the Weiss field and

Table 1. List of major AF materials and their Néel temperatures (T_N). After [15–21].

AF materials	T_N (K)	AF materials	T_N (K)
III–IV: FeO	198	I–VI–III–VI: CuFeO ₂	11
CoO	293	CuFeS ₂	825
NiO	525	CuFeSe ₂	70
III: Cr	311	CuFeTe ₂	254
FeMn	333	III–V: FeN	100
NiMn	797	FeP	115
IrMn	960	FeAs	77
PtMn	702	FeSb	220
II–VI: MnO	122	MnN	660
MnS	152	GdP	15
MnSe	173	GdAs	19
MnTe	323	GdSb	27
EuSe	5	II–V–IV–V: MnSiN ₂	490
EuTe	10	I–II–V: LiMnSb	>RT

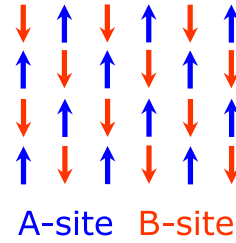


Figure 2. Schematic AF configuration of magnetic moments.

C is the Curie constant. This provides a total magnetisation as follows:

$$M = M_A + M_B = \frac{C}{T} [(H - wM_A - w'M_B) + (H - w'M_A - wM_B)]$$

$$\therefore M = \frac{C}{T} [2H - (w + w')M]. \quad (2)$$

Therefore, the corresponding magnetic susceptibility can be calculated as

$$\chi = \frac{M}{H} = \frac{C}{T + \frac{C}{2}(w + w')} = \frac{C}{T + T_N}. \quad (3)$$

Here, w and w' represent the Weiss field constants within the same site and across the sites, respectively. At $T = T_N$, M becomes zero. T_N can be determined by measuring the temperature dependence of magnetic susceptibility. However, for AF thin films, this determination cannot provide an accurate determination of T_N due to their small volumes.

To characterise an AF material, especially in its thin-film form attached to an FM layer, H_{ex} has been commonly employed. First, Meiklejohn and Bean assumed a perfect AF/FM interface with uncompensated interfacial spins to induce exchange coupling but their calculations were orders of magnitude above measured values. AF domain walls were then considered at the interface to explain the reduced effective exchange coupling [19]. However, the domain-wall model assumed the rotation of moments along the plane normal, which cannot explain H_{ex} for a thin AF film with a small

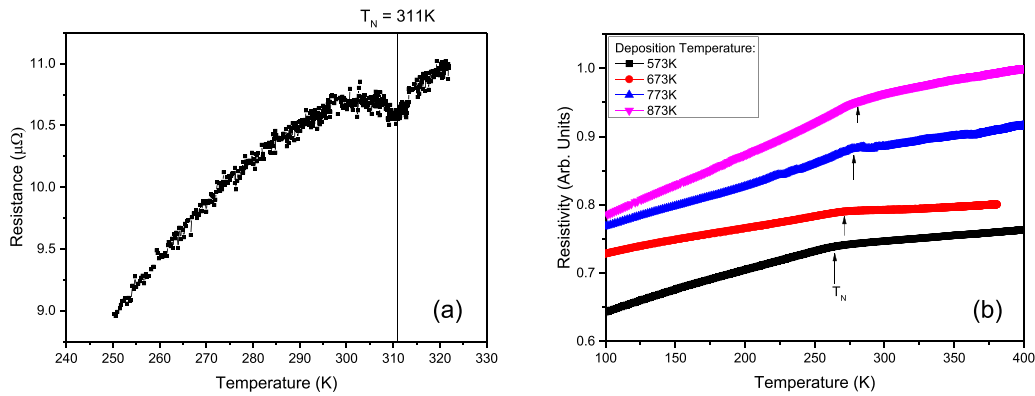


Figure 3. Temperature-dependent resistivity of (a) a single-crystal Cr foil and (b) 100 nm-thick Ni_2MnAl films.

moment deviation. Later, Malozemoff *et al* considered the effect of interface roughness on an otherwise compensated AF/FM interface [21]. The roughness can lead to the formation of AF domains as long as their size is smaller than the AF grain size. Koon investigated the role of a so-called spin-flop coupling [23]. However, this coupling alone does not give rise to exchange bias. Defects in the AF, however, can lead to the formation of AF domains. Model calculations of the so-called domain-state model show qualitative agreement with many experimental results [25]. A model which focuses on polycrystalline AF samples was proposed by Fulcomer and Charap based on the Stoner–Wohlfarth theory [27]. Thermal fluctuations of the grain magnetisation was taken into account and energy distributions were calculated. By extending the Fulcomer–Charap model with time (t)-dependence, the York model of exchange bias has been proposed recently [28].

In polycrystalline films the AF is set below T_N to avoid damage to the AF/FM structure. The AF layer is ordered by the exchange field from the FM layer. This is done by field annealing using thermal activation giving an $\ln(t)$ process. Temperature also causes parts of the AF to disorder and only the stable grains induce H_{ex} . For Ir–Mn, where $T_N = 960$ K, the setting of the AF layer is often incomplete. Using this macroscopic model, temperature dependence of the magnetisation curves can be reproducibly measured using the York protocol [28]. In the corresponding York protocol, the AF is set at the setting temperature (T_{SET}) for 90 min, which is above T_N of the AF film but below the Curie temperature (T_C) of the FM film. The sample is then cooled to the thermally activated temperature (T_{NA}). The sample is heated to the activation temperature (T_{ACT}) for 30 min and is measured at T_{NA} . A period of 30 min would reverse any activated grains to their original ‘set’ state. These times also negate any thermal activation that may occur during the temperature rise and fall. This procedure removes the first loop training effect and measuring at T_{NA} ensures that slow thermal training does not occur. In polycrystalline systems, individual grains have their own blocking temperature (T_B), which can be determined by increasing the activation temperature until the loop shift becomes zero. By continuously elevating T_{NA} , T_{ACT} becomes T_{SET} , which represents the median value of T_B ($\langle T_B \rangle$), which is the temperature when the reversed AF volume is equal to that of the initially set volume. $\langle T_B \rangle$ is an indicative measure of T_N .

More directly, the temperature dependence of electrical resistivity has been utilised to determine T_N by detecting its gradient change [29]. Above T_N , the moment alignment becomes random in the AF materials and changes the corresponding resistivity. As a reference, a single-crystal of Cr with dimensions $5 \times 5 \times 1$ mm³ has been measured to confirm the applicability of the resistivity measurements to determine T_N in a thin film form. A clear minimum is observed in the resistivity at 311 K as shown in figure 3(a). It is important to note that the change in resistance at T_N is of the order of $\mu\Omega$. Measuring this change is only possible due to the low resistance of the crystal and it is unlikely that this technique can be applicable to thin polycrystalline films. 100 nm-thick epitaxial Ni_2MnAl films have then been grown using magnetron sputtering and measured using the same technique [30]. A change in the gradient is observed between 265 and 280 K dependant on their growth temperatures. These changes in the gradient are due to a magnetic phase change of Ni_2MnAl as expected, allowing us to estimate T_N with different growth temperatures. T_N is found to increase with increasing growth temperatures and resulting crystalline ordering. Hence, the temperature-dependent resistivity measurement is a powerful technique to determine T_N for epitaxial or highly-textured films. It should be noted that the changes in the resistivity among these samples are found to be 11% maximum, while those between epitaxial and polycrystalline films are measured to be over three orders of magnitude due to significant electron scattering at grain boundaries in the latter films.

In order to characterise the AF materials microscopically, synchrotron radiation has been widely employed. X-ray magnetic linear dichroism (XMLD) utilises a pair of linearly polarised soft x-ray beams with perpendicular polarisation axes, which is different from a pair of circularly polarised beams used in x-ray magnetic circular dichroism (XMCD) [31, 32]. Here, XMCD signals are proportional to the average value of a magnetic moment in a domain ($\langle M \rangle$), while XMLD signals are proportional to $\langle M^2 \rangle$. For an AF material, $\langle M \rangle$ is zero as $M_A = -M_B$ within an AF domain in equation (2), resulting in no XMCD signal. However, $\langle M^2 \rangle$ is a finite value for an AF material, allowing AF domain imaging. For example for an Fe/NiO bilayer, NiO domain structures have been observed by taking a Ni L -edge, which is strongly affected by the exchange

Table 2. List of major AF and CF Heusler alloys and their Néel temperatures (T_N), Curie temperatures (T_C), average blocking temperatures ($\langle T_B \rangle$), exchange biases (H_{ex}) and their forms, bulk, epitaxial (epi.) or polycrystalline (poly.) films or calculations (calc.). Simulated results using molecular dynamics (MF) are also shown.

Alloys	T_N (K)	T_C (K)	$\langle T_B \rangle$ (K)	H_{ex} (Oe)	Forms	References
Pt ₂ MnGa	350	—			Bulk	[36]
Ru ₂ MnGe	300	—			Bulk	[37]
	320	—	126	680 (10 K)	Simulations	
	365	—			Epi. films	[38]
Ru ₂ MnSi	313	—			Calc.	[39]
	335	—			Calc.	
					Simulations	
Ru ₂ MnSn	296	—				
Ru ₂ MnSb	195	—				
Ni ₂ MnAl	313	—			Bulk (B2)	[40]
	—	375			Bulk (L2 ₁)	
	245	—			Calc. (B2-I)	[41]
	350	—			Calc. (B2-II)	
	—	368			Calc. (L2 ₁)	
	340	—			Calc. (B2-I)	[42]
	372	—			MF calc.	
	220	—			Calc. (B2-II)	
	352	—			MF calc.	
	285	—			Calc. (B2-II)	
	280	—		>55 (10 K)	Epi. films	[30]
Mn ₂ VAl	>600	—			Bulk	[43]
	>RT	—	~200	120 (10 K)	Epi. films	
	360	—			Calc.	
	636	—			MF calc.	
Mn ₂ VSi	—	—	<100	34 (100 K)	Poly. films	[44]
Mn ₃ Ga	470	—			Bulk	[45]
	648	—	~400	1.5k (RT)	Epi. films	[46]
	—	—	235	430 (120 K)	Poly. films	[47]
Mn _{3.04} Ge _{0.96}	—	—	390			[48]
	—	—				[49]
Mn _{2.4} Pt _{0.6} Ga	—	~90		33k (2 K)	Bulk	[50]
	—	—		0 (90 K)		
Mn _{1.8} FeGa	—	~350		12k (2 K)	Bulk	
	—	—		~300 (RT)		
Mn _{2.5} Co _{0.3} Ga _{1.2}	—	—	>350	250 (RT)	Poly. films	
MnN	660	—	388	1475 (RT)	Poly. films	[51]
	570	—			Calc.	
Fe ₂ VAl	—	—			Calc.	[52]
	—	—			Poly. films	[53]
Cr ₂ MnSb	342	—			Calc.	[54]

coupling between Fe and NiO (spin image), and by taking the O *K*-edge, which is originated from the intrinsic AF anisotropy due to the strong coupling with the Ni 3*d* orbital (twin image) [33]. For these domain imaging, a large uniform domain (>a few μm) is required, which makes it difficult to be used for an AF thin films.

Polarised neutron reflectivity (PNR) is another synchrotron-based technique to determine magnetic properties of bulk and layered materials [34]. Due to the magnetic moment of neutron beam interacting with magnetic materials to be observed, not only layer structures, such as thickness, density, composition and interfacial roughness, but also in-plane magnetic moments can be measured. The former structural analysis is

similar to x-ray reflectivity (XRR) measurements but with higher accuracy in a shorter scanning period (<1 min.). The latter magnetic information can be obtained by detecting the neutron reflection with its spins interacted with those in an AF and/or FM layers.

In order to develop a replacement for Ir–Mn, RT antiferromagnetism needs to be achieved, which can be confirmed by the above techniques. To achieve this, three criteria needs to be satisfied: (i) H_{EB} should be greater than 1 kOe at RT, (ii) $\langle T_B \rangle$ should be above RT and (iii) the standard deviation of $\langle T_B \rangle$ should be less than 0.3 K. As listed in table 1, however, the majority of the AF materials have T_N near or below RT. Even though some oxides (e.g. NiO) and sulphides (e.g.

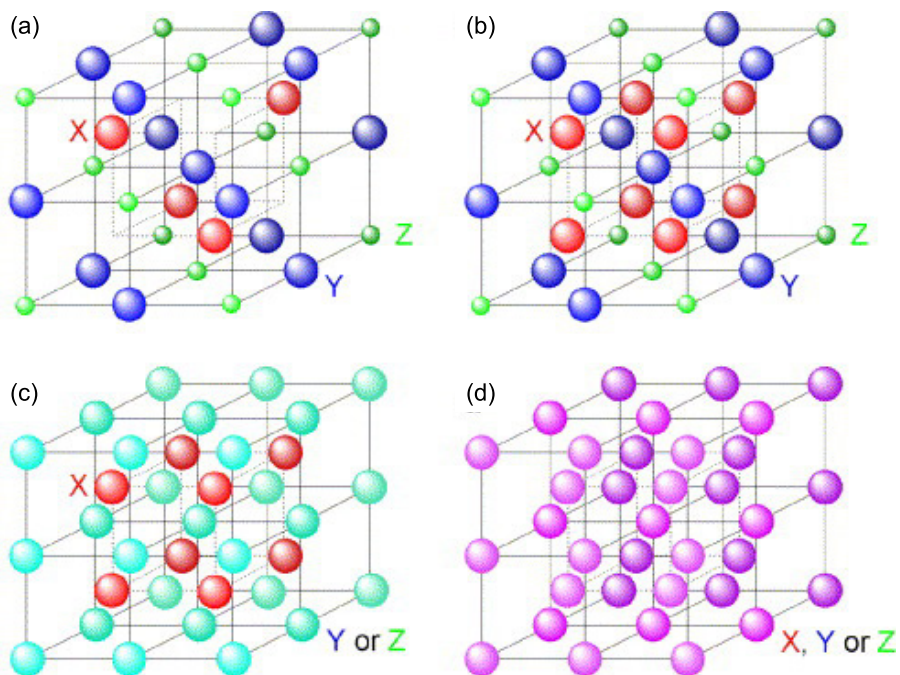


Figure 4. Crystalline ordering of Heusler alloys: (a) half-Heusler alloy with the $C1_b$ phase and full-Heusler alloy with the (b) $L2_1$, (c) $B2$ and (d) $A2$ phases [55].

H																	Z	He
Li	Be											B	C	N	O	F	Ne	
Na	Mg	Y					X					Al	Si	P	S	Cl	Ar	
K	Ca	Sc	Ti	V	Cr	Mn	Fe	Co	Ni	Cu	Zn	Ga	Ge	As	Se	Br	Kr	
Rb	Sr	Y	Zr	Nb	Mo	Tc	Ru	Rh	Pd	Ag	Cd	In	Sn	Sb	Te	I	Xe	
Cs	Ba		Hf	Ta	W	Re	Os	Ir	Pt	Au	Hg	Tl	Pd	Bi	Po	At	Rn	
Fr	Ra																	
		La	Ce	Pr	Nd	Pm	Sm	Eu	Gd	Tb	Dy	Ho	Er	Tm	Yb	Lu		
		Ac	Th	Pa	U	Np	Pu	Am	Cm	Bk	Cf	Es	Fm	Md	No	Lr		

Figure 5. Major combinations of Heusler alloys [55].

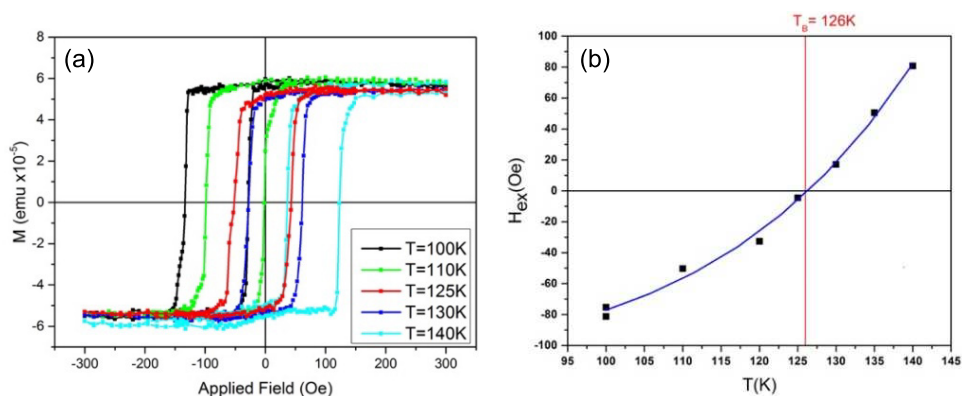


Figure 6. (a) Hysteresis loops showing the reversal of exchange bias of Ru_2MnGe/Fe sample. (b) H_{ex} obtained for Ru_2MnGe in a reversed cooling experiment as a function of temperature.

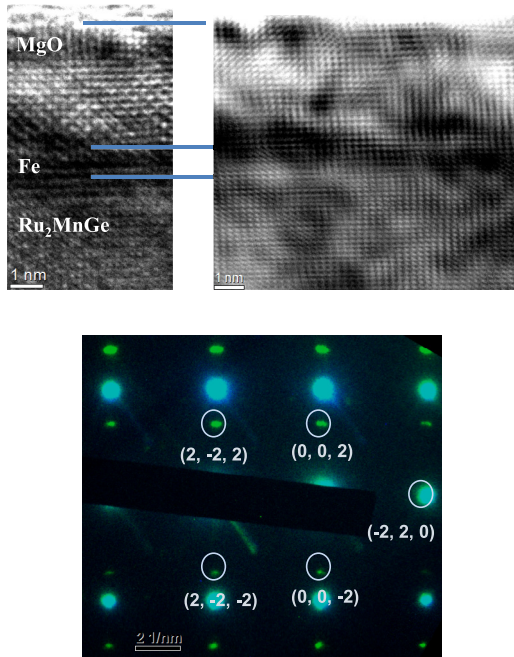


Figure 7. Cross-sectional TEM images of epitaxial $\text{Ru}_2\text{MnGe}/\text{Fe}$ layers with the corresponding selected area electron diffraction (SAED) pattern.

CuFeS_2) have $T_N > \text{RT}$, they have very poor corrosion resistance and hence cannot be used for the Ir–Mn replacement. Manganese alloys (e.g. NiMn and PtMn) and nitrides (e.g. MnN and MnSiN_2) also have $T_N > \text{RT}$. However, NiMn has poor corrosion resistance and PtMn has very high crystallisation temperature, indicating that they cannot be used in commercially available devices as replacements for Ir–Mn. Therefore, new AF Heusler alloys [35], including nitride compounds in their wider definition, need to be developed for the Ir–Mn replacement.

3. Development of antiferromagnetic Heusler alloys

A list of major AF and compensated ferrimagnetic (CF) Heusler alloys is shown in table 2. The Heusler alloys are categorised into two types: (i) full- and (ii) half-Heusler alloys. These alloys crystallise in (i) $L2_1$ phase with X_2YZ composition and (ii) $C1_b$ phase with XYZ composition as shown in figure 4, respectively [55]. The half-Heusler alloys have an X-vacancy in the unit cell, making it to be susceptible to atomic displacement. Even for the full-Heusler alloys, the perfectly-ordered $L2_1$ phase can be deformed into the $B2$ phase by atomically displacing Y–Z elements, the $D0_3$ phase by X–Y displacements and the $A2$ phase by randomly exchanging X–Y–Z elements. The degree of crystallisation in the full-Heusler alloy films can be quantified based on the intensity and width of the (220) principal peaks in x-ray or electron-beam diffraction, indicating the formation of the $A2$ phase. The coexistence of both the (220) and (200) peaks can indicate the formation of the $B2$ crystalline ordering. The existence of the additional (111) peak confirms some degree of the formation of the perfectly ordered $L2_1$ crystalline phase.

As shown in figure 5, the Heusler alloys can be formed with the X and Y atoms to be transition metals and the Z atom to be a semiconductor or a non-magnetic metal. These combinations provide more than 2500 Heusler alloys. In addition, constituent elements in a Heusler alloy can be substituted by the other elements, offering great opportunity for the development of a new AF material [56]. In particular, by counting the total number of valence electrons, the atomic substitution is known to maintain the corresponding magnetic properties to satisfy the generalised Slater-Pauling curve. This allows the continuous engineering of the AF properties in the Heusler alloys with controlling their lattice constants and associated crystalline anisotropy.

In Heusler alloys, half-Heusler alloys have low Néel temperatures in general. For example, CuMnSb [57], NdBiFe [58] and GdPdBi [59] have their T_N to be 55, 2.18 and 13 K, respectively. These are not suitable for Ir–Mn replacement in spintronic devices due to their low $T_N < \text{RT}$ and due to the use of rare materials in the latter two alloys. Therefore, full-Heusler alloys have been focused for the development of AF films with their $T_N > \text{RT}$.

As listed in table 2, Fe_2VAI , where Y and Z elements can be substituted with any other elements as listed in figure 5, has been predicted to have a tendency to form a spin-glass (form AF ordering in $\text{Fe}_{2.5}\text{V}_{0.5}\text{Al}$) [52]. Mn_2VAI is analogous to Fe_2VAI but replaces the Fe with the very high moment Mn. These alloys can be further engineered by substituting some of Mn atoms with the other high-moment atoms to form $(\text{Co},\text{Mn})_2\text{VAI}$ for instance, which is analogous to the other two families with the exception that the element denoted X is now replaced by a mixture of two high moment atoms. By replacing V with Mn, low-moment-based alloys, e.g. Ni_2MnAl , are anticipated to have a high compensated moment. By utilising a heavier element as a base of the Heusler alloys, Ru_2MnAl is expected to have the potential advantage of having both X and Y as the high moment atoms. These families are anticipated to exhibit AF ordering. For RT antiferromagnetism, the AF phase should be stabilised by introducing larger anisotropy and larger AF grain volume. Recently, perpendicularly magnetised FM has also been reported to be pinned by IrMn layer [60]. Hence, the introduction of the additional tetragonal distortion into the cubic Heusler alloys may be necessary for the development of a RT AF.

3.1. Ru-based Heusler alloys

Epitaxially grown Ru_2MnGe films have a very small lattice mismatch of 0.5% on a $\text{MgO}(001)$ substrate with the relationship, $\text{Ru}_2\text{MnGe}[100](001) \parallel \text{MgO}[110](001)$ ($a_{\text{Ru}_2\text{MnGe}} = 0.5985 \text{ nm}$ and $a_{\text{MgO}} = 0.5957 \text{ nm}$). At a substrate temperature $T_{\text{sub}} > 400 \text{ }^\circ\text{C}$, the formation of epitaxial films has been reported [38]. The optimum growth temperature has been reported to be $T_{\text{sub}} = 500 \text{ }^\circ\text{C}$, where the diffraction peaks and their Laue oscillations are most pronounced. At higher temperatures, Mn starts to evaporate from the sample. The calculated lattice constant deduced from the (200) and (400) peak positions in x-ray diffraction (XRD) measurements

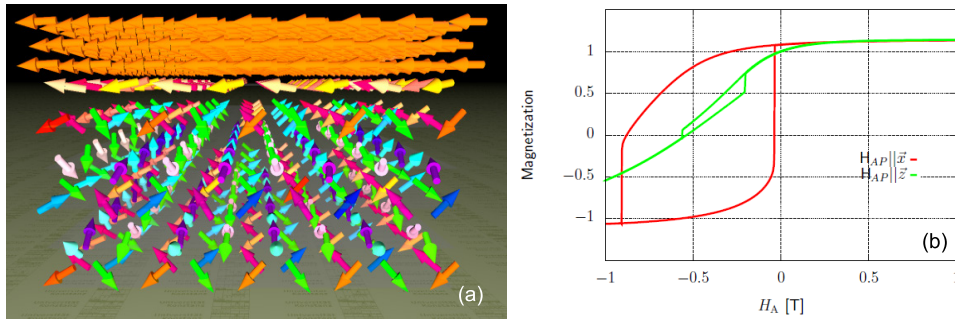


Figure 8. (a) Sketch of the magnetic state after in-plane field-cooling for a Ru_2MnSi (L_{21})/Fe interface. (b) In-plane and out-of-plane hysteresis loops of the Ru_2MnSi (L_{21})/Fe bilayers at 0 K [42].

is $c = 0.6041$ nm. Considering a 1% tetragonal distortion induced by the compressive strain from the lattice mismatch, the lattice constant matches the prediction if the unit cell volume is held constant.

Figure 6 shows a series of hysteresis loops for a sample with an epitaxial $\text{Ru}_2\text{MnGe}/\text{Fe}$ bilayer measured following the same experimental procedure as used for a granular AF/FM system [28]. As can be seen, progressive thermal activation leads to a reversal of the exchange bias as shown in figure 6(a). This allows for the distribution of T_B to be calculated as shown by the line in figure 6(b), showing $\langle T_B \rangle = 126$ K.

The optimum epitaxial $\text{Ru}_2\text{MnGe}/\text{Fe}$ bilayers have been imaged using cross-sectional transmission electron microscopy (TEM). Both substrate and FM layer interfaces confirm the lattice matching and crystalline quality. The thin FM layer does not offer enough contrast for TEM studies. The (220) and (200) reflections are observed for the (110) Heusler zone axis. The (222) reflections indicate the formation of the L_{21} phase.

The magnetic state and its dependence on the atomic disorder and chemical composition for Ru_2MnGe have been investigated within a multi-scale approach [61] combining first principles calculations with advanced classical spin model simulations. Based on the first principles calculations, spin models were first parameterised and then, in a second step simulated by means of the stochastic Landau–Lifshitz–Gilbert equation of motion. Hysteretic as well as thermal properties of bilayers of $\text{Ru}_2\text{MnZ}/\text{Fe}$ ($Z = \text{Si}$ or Ge) can thus be obtained.

The Ru-based bilayers show exchange bias in agreement with above measurements. This effect is much stronger than in the Ni-based bilayers as discussed in the following subsection. As figure 8 illustrates for a $\text{Ru}_2\text{MnSi}/\text{Fe}$ interface, exchange bias exists without structural disorder in the antiferromagnet, i.e. for the L_{21} phase. Due to the strong FM coupling between the interface atoms, close to the interface, the Fe and Mn spins are oriented nearly parallel, and the direction of these spins is in-plane following the in-plane magnetic anisotropy. The hysteresis loop calculations show that the magnetisation curve is shifted vertically and horizontally, where the horizontal shift of the hysteresis loops is larger and indicates the H_{ex} effect. Furthermore, simulations at finite temperature indicate a strong thermal dependence, where H_{ex} at $T = 100$ K is less than a quarter of the corresponding value at $T = 0$ K. This also agrees with the relatively small H_{ex} measured only at low temperature. The $\text{Ru}_2\text{MnGe}/\text{Fe}$ bilayers show a similar

Table 3. Calculated magnetic moments (m_{Mn}), K^{os} , K^{ts} and MAE for Ru_2MnGe with tetragonal lattice distortion.

	m_{Mn} (μ_B)	K^{os} (meV)	K^{ts} (meV)	MAE = $K^{\text{os}} + K^{\text{ts}}$ (meV)
$c/a = 1.00$	2.91	9.7×10^{-5}	-2.7×10^{-4}	-1.8×10^{-4}
$c/a = 1.05$	2.88	0.32	0.21	0.53
$c/a = 1.10$	2.79	0.54	0.41	0.95
$c/a = 1.15$	2.65	0.55	0.82	1.37
$c/a = 1.20$	2.49	0.43	0.80	1.23

complex magnetic structure which is more sensitive to the presence of an applied field in comparison to the $\text{Ru}_2\text{MnSi}/\text{Fe}$ bilayer, in part because the on-site anisotropy is reduced. The exchange bias effect is smaller.

These results confirm that the Ru-based Heusler alloys require to be in the L_{21} phase to exhibit AF behaviour. In order to increase the AF anisotropy and with that H_{ex} , a lattice distortion was considered as well. The calculated spin moments and magnetic anisotropy energies (on-site: K^{os} , two-site: K^{ts} , the sum of them: magnetic anisotropy energy (MAE)), are listed in table 3 for different c/a ratios in Ru_2MnGe . Note that 1 meV equals to 8.21×10^6 erg cm^{-3} . For Ir–Mn(110) MAE is measured to be 3.2×10^5 erg cm^{-3} and $H_{\text{ex}} = 360$ Oe [62], which is comparable to MAE for $c/a > 1.05$. These calculated results suggest that tetragonal distortion (stretching) induces large uniaxial anisotropy in Ru_2MnZ due to a combined effect of symmetry breaking and spin–orbit coupling. It should be noted that a similar AF behaviour has been reported for the other heavy-metal-based Heusler alloys, such as Pt_2MnGa [36]. Therefore, for the heavy-metal-based Heusler alloys, high-moment element, e.g. Mn, is necessary to induce AF behaviour. The AF anisotropy can be increased by introducing tetragonal distortion, leading to RT AF behaviour.

3.2. Ni-based Heusler alloys

Ni_2MnAl films grown on $\text{MgO}(001)$ exhibit the superlattice (200) diffraction but no (111) peak in addition to the fundamental (220) diffraction using XRD, which suggests that the films are in the $B2$ phase [30]. The results of XRD φ -scans confirm that all films including the film deposited at RT satisfy the epitaxial relation, $\text{Ni}_2\text{MnAl}[100](001) \parallel \text{MgO}[110](001)$. H_{ex} of 55 Oe is obtained for the RT grown films, while no exchange bias (rather a weak FM signals) is detected for

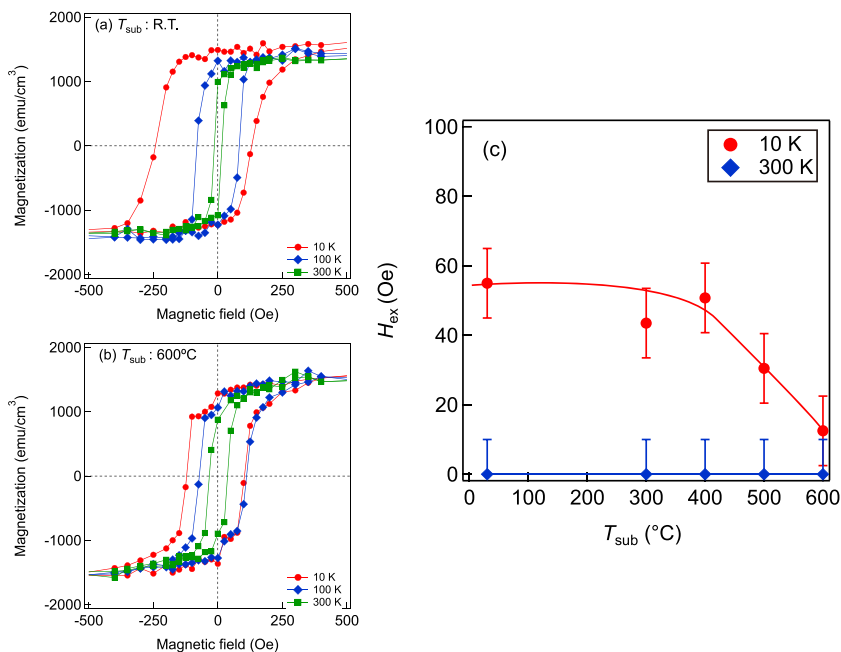


Figure 9. Hysteresis loops showing the reversal of exchange bias of $\text{Ni}_2\text{MnAl}/\text{Fe}$ sample grown at (a) RT and (b) 600°C . (c) H_{ex} obtained for Ni_2MnAl in a reversed cooling experiment as a function of temperature [30].

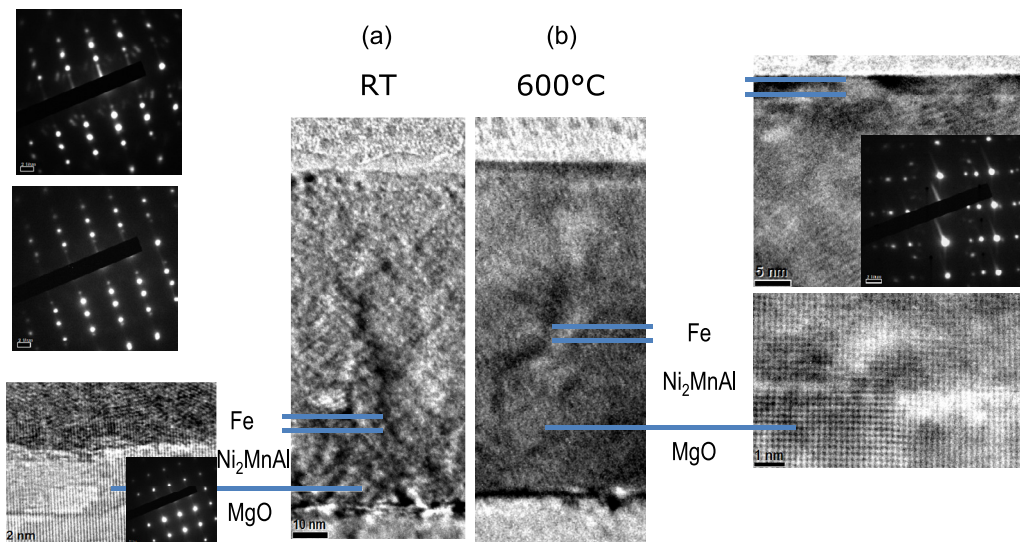


Figure 10. Cross-sectional TEM images of epitaxial $\text{Ni}_2\text{MnAl}/\text{Fe}$ layers grown at (a) RT and (b) 600°C with the corresponding SAED patterns.

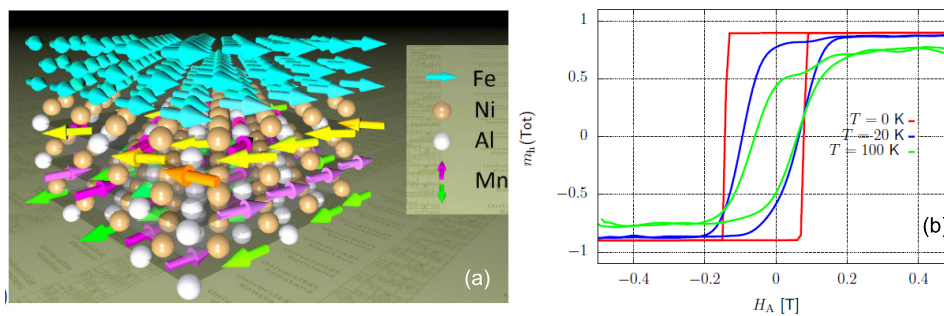


Figure 11. (a) Sketch of the magnetic state after field-cooling for a Ni_2MnAl ($B2\text{-II}$)/Fe interface. (b) In-plane hysteresis loops of the Ni_2MnAl ($B2$)/Fe bilayers at $T = 0; 20$ and 100 K [63].

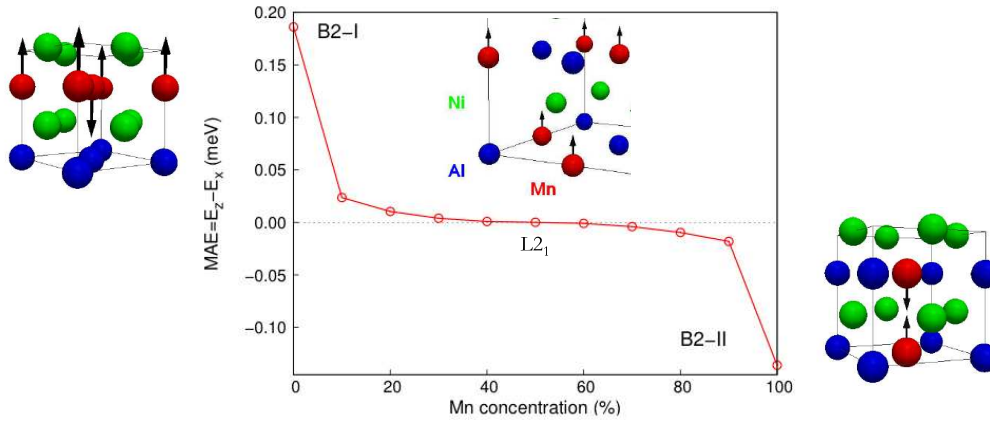


Figure 12. MAE as a function of Mn concentrations in Ni₂MnAl and the corresponding crystalline structures.

Table 4. Calculated MAE for Ni₂MnAl with tetragonal lattice distortion.

	$c/a = 0.90$	$c/a = 0.95$	$c/a = 1.00$	$c/a = 1.05$	$c/a = 1.10$
MAE (meV)	0.054	0.027	0.00	-0.028	-0.059

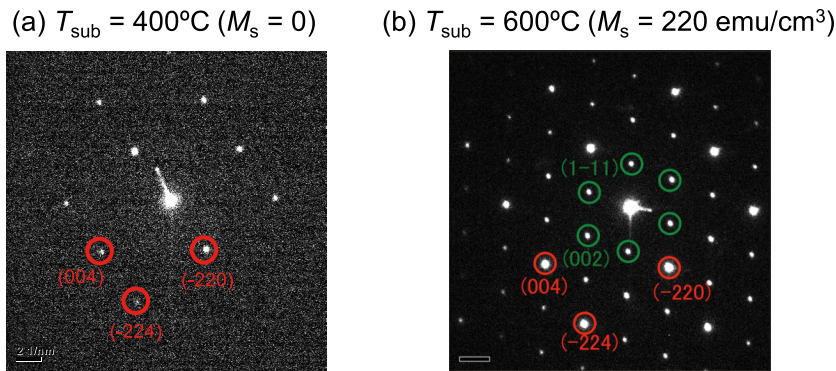


Figure 13. SAED patterns of Mn₂VAl films. (a) $T_{\text{sub}} = 400\text{ }^\circ\text{C}$ and (b) $600\text{ }^\circ\text{C}$.

those grown at higher temperatures, e.g. $600\text{ }^\circ\text{C}$ as shown in figure 9.

To identify the differences between these Ni₂MnAl layers grown at RT and $600\text{ }^\circ\text{C}$, the Ni₂MnAl epitaxial samples have been imaged using cross-sectional TEM. The epitaxially deposited Ni₂MnAl/Fe bilayers exhibit good crystalline structure as seen in figure 10 with sharp interfaces which may exhibit less than three atomic planes in roughness. Here, the Ni₂MnAl films grown at $600\text{ }^\circ\text{C}$ are found to partially form the L₂₁ phase confirmed by the minor presence of the (111) diffraction spots in their SAED image in figure 10. However, those grown at RT form the B2 phase without the (111) spots but with the (220) and (200) spots. By taking the above magnetisation measurements, Ni₂MnAl requires the B2 ordering to exhibit AF behaviour. The Ni₂MnAl layer shows a number of crystalline defects that define a fine granular-like structure due to the local breaking of symmetry within the atomic planes. The random distribution of crystalline boundaries may be detrimental to the thermal stability of AF, as the formation of small single domain structures of around 5nm or less may lead to thermal instability of the material. A

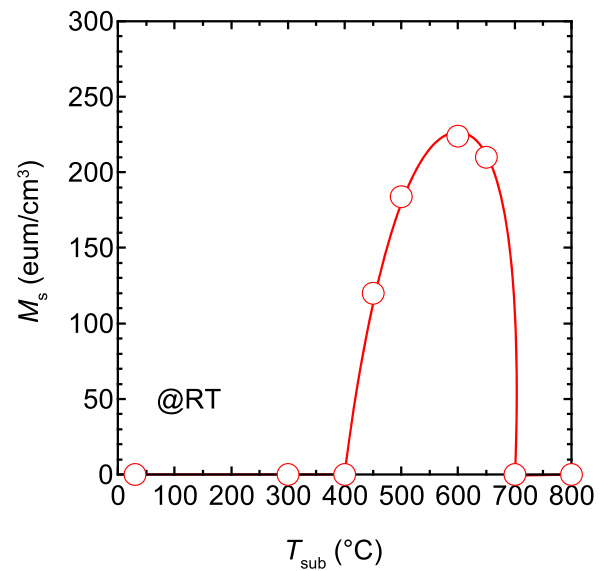


Figure 14. Substrate temperature, T_{sub} dependence of saturation magnetisation, M_s for Mn₂VAl films.

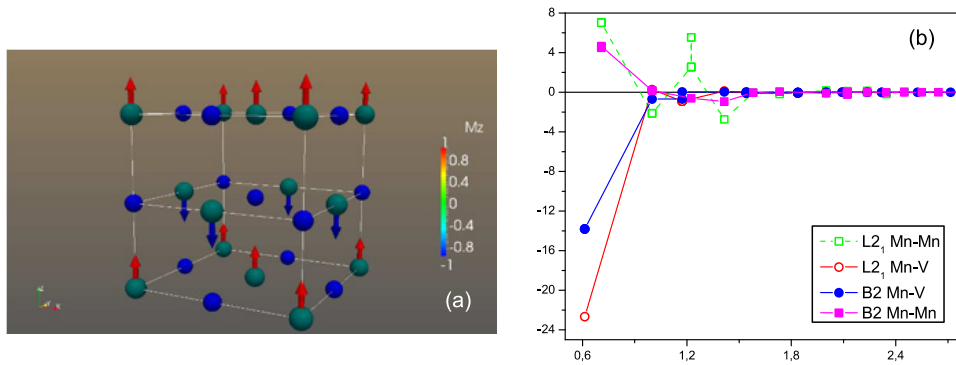


Figure 15. (a) Sketch of the magnetic ground state of Mn_2VAI ($L2_1$) bulk. (b) Calculated Mn–Mn and Mn–V exchange parameters for Mn_2VAI as a function of the inter-atomic distance for the ordered $L2_1$ and the partially disordered $B2$ phases.

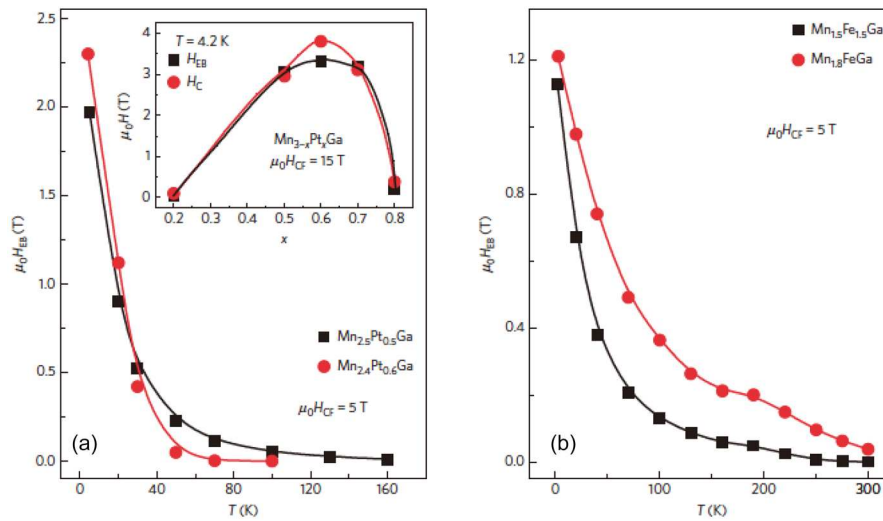


Figure 16. (a) Temperature dependence of H_{ex} for $Mn_{2.4}Pt_{0.6}Ga$ and $Mn_{2.5}Pt_{0.5}Ga$. The inset shows the coercive field H_C and H_{ex} as a function of the Pt concentration x in $Mn_{3-x}Pt_xGa$. (b) Temperature dependence of H_{ex} for $Mn_{1.5}Fe_{1.5}Ga$ and $Mn_{1.8}FeGa$. The lines are guides to the eye [50].

larger grain size and columnar growth are more desirable for increased thermal stability of the AF structure.

In the case of the Ni-based AF in the crystallographically ordered $L2_1$ phase, the atomistic calculations confirm that no exchange bias occurs [63]. However, in that case a spinflop coupling can lead to an enhanced coercivity and to the fact that one can switch the AF with an external field via the coupling to FM. For the partially disordered $B2$ phase of the Ni_2MnAl , a small H_{ex} has been found as shown in figure 11, which agrees with experiments as described above. The reason for the exchange bias effect is a combination of the disorder, which leads to uncompensated spin structures along the interface, with the anisotropy of AF. MAE has been calculated along the path between the ordered $B2$ -I and $B2$ -II structures as a function of Mn concentration on the Al sites (see figure 12). This confirms that short-range order can induce sizeable MAE for $B2$ -II. Since the anisotropy is rather low (an order of magnitude smaller than that for the Ru-based Heusler alloys), H_{ex} is rather small, and depends on the grain volume. It is furthermore rather unstable against thermal fluctuations with a maximum T_B of below 100 K as agreed with the experiment. In order to investigate a potential increase of H_{ex} through a lattice distortion the MAE per

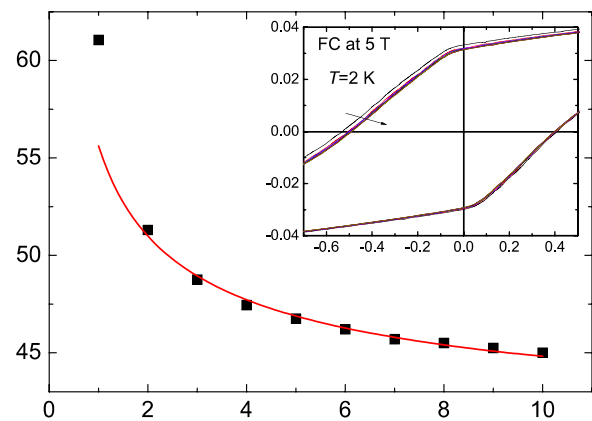


Figure 17. Variation of H_{ex} with number of field cycles n measured at 2 K. The line serves as a guide to the eye. The inset shows the training effect on the $M(H)$ loops [49].

unit cell has been calculated for several values of the c/a ratio in the $B2$ phase (see table 4). Therefore, the Heusler alloys based with a transition metal with a small magnetic moment exhibits their AF phase when the high-moment Y atoms form antiparallel configuration between their second-nearest neighbours.

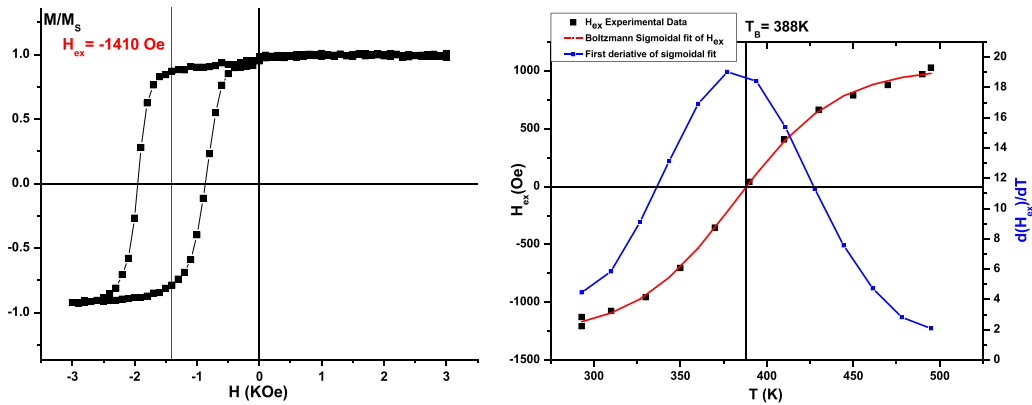


Figure 18. (a) Hysteresis loops showing the reversal of exchange bias of MnN/Fe sample. (b) H_{ex} obtained for MnN in a reversed cooling experiment as a function of temperature.

3.3. Mn-based Heusler alloys

As a Heusler alloy based with a transition metal with a high moment, Mn_2VAI films have been grown onto $MgO(001)$ single crystalline substrates. The superlattice diffraction of the (200) peak appears for the growth temperatures, $T_{sub} = 500$ °C and 600 °C. In addition, these samples exhibit the (111) superlattice diffraction in a pseudo-in-plane scan. These results indicate that the films are in the $L2_1$ phase for $T_{sub} \geq 500$ °C. On the other hand, only the fundamental (400) diffraction appears for the other samples with $T_{sub} \leq 400$ °C, suggesting that the films are in the $A2$ phase. SAED patterns are shown in figure 13 for $T_{sub} = 400$ °C and 600 °C representing the $A2$ phase and $L2_1$ phase, respectively.

Figure 13 shows the T_{sub} dependence of magnetisation values for Mn_2VAI films measured at RT. The films exhibit saturation magnetisations of 190 and 220 $emu\ cm^{-3}$ for $T_{sub} = 500$ °C and 600 °C, respectively. On the other hand, no FM (or FI) magnetic hysteresis loop appears for the other samples with the $A2$ phase, which suggests a possibility to be an AF or CF. The T_{sub} dependence of the chemical phases and magnetisation values are similar with those reported in a previous work [64]. By depositing the optimised Mn_2VAI/Fe bilayer, H_{ex} of 120 Oe at 10K has been measured [43], which decreases rapidly with increasing temperature but is maintained to be ~ 10 Oe at 200K. The corresponding $\langle T_B \rangle$ has been estimated to be ~ 75 K using the York protocol.

PNR experiments has confirmed the presence of an AF phase at RT in a polycrystalline $A2$ -ordered Mn_2VAI bulk sample. The Mn_2VAI sample show an AF peak at the (100) reflection of the $A2$ phase which disappears at around 500 K on top of a broad nuclear reflection peak from the $L2_1$ phase [65]. From another set of neutron diffraction experiments on Mn_2VAI epitaxial films, the film deposited at 400 °C is found to show AF $A2$ phase at RT, while those deposited at room temperature and 600 °C show $A2$ phase without AF ordering and $L2_1$ phase, respectively [43]. The corresponding magnetisation values as shown in figure 14 confirms the crystallisation of the AF (the growth temperature (T_{sub}) < 400 °C) and FI ($T_{sub} > 400$ °C).

The ordered Mn_2VAI alloy has a FI ground state with rather large V moments oriented opposite to the Mn moments. Here

the strong antiparallel Mn–V couplings stabilise the FI state. In order to trace the effect of atomic disorder in the system, the $B2$ phase is calculated as shown in figure 15. Here, the AF coupling between in-plane first nearest neighbour Mn atoms is much weaker than those between out-of-plane Mn atoms, indicating the presence of out-of-plane anisotropy. The disorder between the V and Al atoms does not influence significantly the magnetic state as compared to the ordered $L2_1$ state. The fully disordered $A2$ phase is also studied as a random three-component alloy in terms of single site coherent potential approximation (CPA). The completely disordered $A2$ state is calculated to be non-magnetic at the same lattice constant as for the $L2_1$ phase. Only by increasing the lattice parameter by more than 8% a spontaneous FM state has been formed. The failure of obtaining an AF ground state (in fact, a magnetic ground state) at the experimental lattice constant indicates that magnetism collapses when a homogeneous atomic disorder is supposed like with the CPA and, most possibly, atomic short-range order (e.g. clustering of Mn atoms) would stabilise the magnetic order in the system.

For the Mn-based Heusler alloys, off-stoichiometric compositions have also been investigated, which confirms the robustness of the Mn-based alloys against their atomic disorder. By taking two FI Heusler alloys, Mn_3Ga and Mn_2PtGa , their compensation point, $Mn_{2.4}Pt_{0.6}Ga$, has been calculated and demonstrated experimentally [50]. As shown in figure 16(a), a local FM domain can be exchange biased by a neighbouring AF domain within such compensated FI, inducing H_{ex} of 33 kOe at 2K. In a similar system of $Mn_{1.8}FeGa$, H_{ex} is reported to survive to be ~ 300 Oe up to RT (see figure 16(b)).

By further substituting Y elements with Mn, binary Heusler alloys can be formed. One example is hexagonal Mn_3Ge [49]. H_{ex} of up to 520 Oe is measured at the boundaries between AF and FM domains as shown in figure 17. Similar off-stoichiometric AF Heusler alloys are reported as Fe_2VAI and Cr_2MnSb . Even though these results may not be directly compared with those for the AF/FM bilayers, these alloys may be used as new AF layers. A tetragonal Mn_3Ga film has then been investigated to induce AF behaviour [45]. A bilayer of epitaxial Mn_3Ga (10 nm)/ $Co_{0.9}Fe_{0.1}$ (2.5 nm) is reported to show H_{ex} of 1.5 kOe at RT. MAE and $\langle T_B \rangle$ are estimated to be 3×10^6 erg cm^{-3} and ~ 400 K, respectively. Recently, H_{ex} of

430 Oe at 120 K in polycrystalline $\text{Mn}_3\text{Ga}/\text{Co}_{0.6}\text{Fe}_{0.4}$ bilayers, confirming the applicability of such binary Heusler alloys for the replacement of Ir–Mn.

By further expanding the definition of the Heusler alloys to nitrides [37], MnN has been investigated. MnN films are grown using ultrahigh vacuum sputtering in N_2 atmosphere to achieve Mn:N = 1:1. A MnN/Fe bilayer has been reported to show H_{ex} of 1.4 kOe at RT with $\langle T_{\text{B}} \rangle = 388$ K as shown in figure 18 [51]. This satisfies the requirements for the Ir–Mn replacement. However, the minimum thickness of MnN to induce the AF behaviour is 20 nm, which needs to be at least halved to be competitive against the 6 nm-thick Ir–Mn layer used in spintronic devices.

Therefore, high-moment-metal-based Heusler alloys display AF behaviour possibly due to the clustering of the high-moment metals even in their disordered A2 phase. MAE is demonstrated to be increased by introducing tetragonal distortion into the unit cell of the alloys. Further engineering in distortion and AF domain size can increase $\langle T_{\text{B}} \rangle$ and H_{ex} of these alloys, allowing the replacement for Ir–Mn alloys used in spintronic devices.

4. Conclusion

Ru_2YZ , Ni_2YZ and Mn_2YZ Heusler alloys have been found to exhibit AF behaviour in their $L2_1$, B2 and A2 crystalline ordering phases. By attaching a FM Fe layer to these AF layers, H_{ex} of up to 680 Oe at 3 K (Ru_2MnGe), 90 Oe at 10-K (Ni_2MnAl) and 120 Oe at 10K (Mn_2VAl) for Ru_2MnGe , Ni_2MnAl and Mn_2VAl , respectively. Mn_2VAl is found to maintain its AF properties at RT. These differences are found to be induced by the AF alignment of spin moments at the Y site in unique ordering phases. In the ordered $L2_1$ type Ru_2MnZ ($Z = \text{Si}, \text{Ge}, \text{Sn}$ or Sb), the complex AF ordering (2nd type) is a consequence of the frustrated exchange interaction between the Mn atoms. It is concluded that T_{N} sharply depends on the Z element and that T_{N} in Ru_2MnGe can be increased by avoiding the disorder in the Mn-Z sub-lattice. For Ni_2MnAl , the (checkerboard-like) AF order only exists in the chemically disordered B2 phase due to the large AF nearest neighbour Mn–Mn interaction. Decreasing the atomic disorder in the Mn–Al sublattice leads to non-zero total magnetisation (ferromagnet). Moreover, the excess of Mn or Ni does not improve the quality of the AF state. From the device application point of view, Mn-based AF Heusler alloys are ideal due to their robustness against atomic disordering, especially at the interfaces against their neighbouring layers. These findings are useful for future implementation to replace iridium alloys in spintronic devices from their sustainability points of view.

Acknowledgments

The authors would like to thank Dr Asaya Fujita of AIST for fruitful discussion. This work was part-funded through a project, HARFIR (Heusler alloy replacement for Iridium), by the European Commission under the 7th Framework

Programme (FP7-NMP-2013-EU-Japan, Grant Agreement No. NMP3-SL-2013-604398) and by the Japan Science and Technology Agency through its Strategic International Collaborative Research Program. AH, GVF and KOG would also like to thank financial support from the UK EPSRC (EP/M02458X/1), while ES and LS acknowledges the support of the National Research, Development and Innovation Office of Hungary (Project Nos. K115575 and PD120917).

ORCID iDs

Atsufumi Hirohata  <https://orcid.org/0000-0001-9107-2330>

References

- [1] 2014 Communication on the review of the list of critical raw materials for the EU and the implementation of the Raw Materials Initiative (https://ec.europa.eu/growth/sectors/raw-materials/specific-interest/critical_en)
- [2] www.matthey.com/
- [3] www.platinum.matthey.com/documents/new-item/pgm%20market%20reports/pgm-market-report-may-2016.pdf
- [4] www.infomine.com/investment/metal-prices/iridium/all/
- [5] Baldo M A *et al* 1999 *Appl. Phys. Lett.* **75** 4
- [6] Konno H 2006 *Tech. Chem. Times* **199** 13
- [7] Uoyama H *et al* 2012 *Nature* **492** 234
- [8] Mining S *Japanese Patent* 2010-132144
- [9] Néel L 1948 *Ann. Phys.* **3** 137
- [10] Shull C G and Smart J S 1949 *Phys. Rev.* **76** 1256
- [11] Anderson P W 1950 *Phys. Rev.* **79** 350
- [12] Meiklejohn W H and Bean C P 1957 *Phys. Rev.* **105** 904
- [13] Fontana R E Jr *et al* 1997 *US Patent* 5,701,223
- [14] Jungwirth T *et al* 2016 *Nat. Nanotechnol.* **11** 231
- [15] Jungwirth T *et al* 2011 *Phys. Rev. B* **83** 035321
- [16] Máca F *et al* 2012 *J. Magn. Magn. Mater.* **324** 1606
- [17] Lewis F B and Saunders N H 1973 *J. Phys. C: Solid State Phys.* **6** 2525–32
- [18] Mitchell M A and Goff J F 1973 *Phys. Rev. B* **5** 1163–70
- [19] Lentz K *et al* 2007 *Phys. Rev. Lett.* **98** 237201
- [20] Hirota E *et al* (ed) 2002 *Giant Magnetoresistance Devices* (Berlin: Springer)
- [21] Tomeno I *et al* 1999 *J. Appl. Phys.* **86** 3853
- [22] Chikazumi S 1997 *Physics of Ferromagnetism* (Oxford: Clarendon Press) pp 134–59
- [23] Mauri D *et al* 1987 *J. Appl. Phys.* **62** 3047
- [24] Malozemoff A P 1987 *Phys. Rev. B* **35** 3679
- [25] Malozemoff A P 1988 *Phys. Rev. B* **37** 7673
- [26] Koon N C 1997 *Phys. Rev. Lett.* **78** 4865
- [27] Nowak U *et al* 2002 *Phys. Rev. B* **66** 014430
- [28] Fulcomer E and Charap S H 1972 *J. Appl. Phys.* **43** 4190
- [29] O'Grady K *et al* 2010 *J. Magn. Magn. Mater.* **322** 883
- [30] Fukamichi K 2014 *Antiferromagnets* (Tokyo: Kyoritsu)
- [31] Tsuchiya T *et al* 2016 *J. Phys. D: Appl. Phys.* **49** 235001
- [32] Thole B T *et al* 1985 *Phys. Rev. Lett.* **55** 2086
- [33] Alders D *et al* 1998 *Phys. Rev. B* **57** 11623
- [34] Kinoshita T *et al* 2004 *J. Phys. Soc. Japan* **73** 2932
- [35] Bland J A C and Heinrich B (ed) 1994 *Ultrathin Magnetic Structures I* (Berlin: Springer) pp 305–43
- [36] Kübler J 2016 private communications
- [37] Singh S *et al* 2016 *Nat. Commun.* **7** 12671
- [38] Mizusaki S *et al* 2012 *J. Alloys Compd.* **510** 141
- [39] Balluff J *et al* 2016 *J. Appl. Phys.* **118** 243907
- [40] Khmelevskiy S *et al* 2015 *Phys. Rev. B* **91** 094432

- [40] Acet M *et al* 2002 *J. Appl. Phys.* **92** 3867
- [41] Galanakis I *et al* 2011 *Appl. Phys. Lett.* **98** 102514
- [42] Yanes Díaz R *et al* 2017 private communications
- [43] Tsuchiya T *et al* arXiv:1707.06731
- [44] Wu H *et al* 2017 *J. Phys. D: Appl. Phys.* **50** 375001
- [45] Krén E and Kádár G 1970 *Solid State Commun.* **8** 1653
- [46] Kurt H *et al* 2012 *Appl. Phys. Lett.* **101** 232402
- [47] Wu H *et al* 2017 *Appl. Phys. Lett. Mater.* submitted
- [48] Kadar G and Kren E 1971 *Int. J. Magn.* **1** 143
- [49] Quian J F *et al* 2014 *J. Phys. D: Appl. Phys.* **47** 305001
- [50] Nayak A K *et al* 2015 *Nat. Mater.* **14** 679
- [51] Meinert M *et al* 2015 *Phys. Rev. B* **92** 144408
- [52] Singh D J and Mazin I 1998 *Phys. Rev. B* **57** 14352
- [53] Huminiuc T *et al* 2017 *J. Magn. Magn. Mater.* in preparation
- [54] Galanakis I *et al* 2007 *Phys. Rev. B* **75** 172404
- [55] Hirohata A *et al* 2006 *Curr. Opin. Solid State Mater. Sci.* **10** 93
- [56] Felser C and Hirohata A (ed) 1970 *Heusler Alloys* (Berlin: Springer)
- [57] Endo K 1970 *J. Phys. Soc. Japan* **29** 643
- [58] Müller R A *et al* 2015 *Phys. Rev. B* **92** 184432
- [59] Jesus C B R *et al* 2014 *Solid State Commun.* **177** 95
- [60] Chen J Y *et al* 2014 *Appl. Phys. Lett.* **104** 152405
- [61] Yanes Díaz R *et al* 2013 *Phys. Rev. Lett.* **111** 217202
- [62] Takanashi M and Tsunoda M 2002 *J. Phys. D: Appl. Phys.* **35** 2365
- [63] Yanes Díaz R *et al* 2017 *Phys. Rev. B* **96** 064435
- [64] Kubota T *et al* 2009 *Appl. Phys. Lett.* **95** 222503
- [65] Umetsu R Y 2017 private communications